Corrosion behaviour of alumina-forming heat resistant alloy with Ti in high temperature steam

Obulan Subramanian, Gokul; Kim, Chaewon; Heo, Woong; Jang, Changheui

DOI:
10.1016/j.corsci.2021.110000

Document Version
Peer reviewed version

Citation for published version (Harvard):
Obulan Subramanian, G, Kim, C, Heo, W & Jang, C 2022, 'Corrosion behaviour of alumina-forming heat resistant alloy with Ti in high temperature steam', *Corrosion Science*, vol. 195, 110000. https://doi.org/10.1016/j.corsci.2021.110000

Corrosion behaviour of alumina-forming heat resistant alloy with Ti in high temperature steam

Gokul Obulan Subramanian[a,b], Chaewon Kim[a], Woong Heo[a], Changheui Jang[a,*]

[a] Korea Advanced Institute of Science and Technology, Daejeon, 34141, Rep. of Korea

[b] University of Birmingham, Birmingham, B15 2TT, United Kingdom

g.subramanian@bham.ac.uk, kcw9591@kaist.ac.kr, hw960306@kaist.ac.kr

*Corresponding author

E-mail: chjang@kaist.ac.kr

Abstract

The corrosion behaviour of an alumina-forming heat resistant alloy with high Ti (Fe-35Ni-16Cr-4.5Al-3Ti, wt.%) was evaluated in high temperature steam. The alloy developed interfacial α-Al_2O_3 layer during the pre-oxidation treatment in air at 750 ^oC. However, it formed external Cr_2O_3 and internal γ-Al_2O_3 oxides on the austenite matrix during the steam corrosion at 750 ^oC for 1000 h. This behaviour is attributed to the increased oxygen permeability into the austenite matrix from the synergistic effect of steam and Ti. Meanwhile, the pre-oxidized alloy with interfacial α-Al_2O_3 layer showed improved corrosion protection with reduced weight gain in steam environment.

Keywords: Alumina-forming alloy; Steam; High temperature corrosion; Pre-oxidation; Internal oxidation;

1. Introduction

The fossil power plants typically use the steam Rankine cycle for power generation, in which the thermal efficiency can be improved by increasing the operating temperature and pressure. The advanced ultra-supercritical (A-USC) power plants target to achieve thermal efficiency above 50 % with steam temperature around 700–760 ^{o}C [1]. The heat resistant alloys for A-USC applications rely on the formation of protective oxide layers to resist the environmental degradation. Typically, the heat resistant alloys utilize the formation of chromia (Cr_2O_3) layer for high temperature corrosion resistance. However, it is known that the chromia-forming alloys are susceptible to increased corrosion rate in water vapour containing environments [2]. The increased corrosion of structural materials in aggressive environments can potentially reduce the creep rupture life of chromia-forming alloys [3], thereby affecting the structural integrity. Meanwhile, alloys with sufficient Al content can form protective alumina (Al_2O_3) layer at higher temperatures, which exhibits significantly reduced growth rate than chromia layer [4], thus provides better corrosion resistance in water vapour containing environments [5, 6].

Recently, the Fe-Ni-based austenitic alumina-forming alloys (AFAs) with 2.5–4 wt.% Al were developed by Oak Ridge National Laboratory (ORNL) for improved corrosion resistance in high temperature environments [7-10]. Several reports on the high temperature corrosion behaviour of AFA were performed in air with 10 % water vapour environment at 800 ^{o}C, which showed the formation of protective Al_2O_3 layer resulting in lower weight gain [7, 10-13]. However, only few corrosion studies were performed on AFAs in pure steam environment at temperatures around 750 ^{o}C relevant to the A-USC plants. The AFA OC4 alloy with 14 wt.% Cr and 3.5 wt.% Al formed highly stable Al_2O_3 layer when exposed to steam at 800 ^{o}C and 1.7 MPa [14]. In addition, the AFA with 17 wt.% Cr and 3.3 wt.% Al showed good corrosion performance in steam at 700

^{o}C, while other AFAs with lower Cr and Al content suffered higher weight gain from internal oxidation [15]. Further analysis on the high temperature corrosion behaviour of AFAs in steam is required to validate its potential application in A-USC plants.

It has been reported that the addition of Ti to AFAs improved the creep life with increased fraction of γ'-Ni_3(Al,Ti) precipitates, however the corrosion resistance was reduced [9, 11]. The addition of beneficial minor elements (C and B) was reported to improve the corrosion resistance of Ti-containing AFA with 3 wt.% Al in air with 10 % water vapour environment at 800 ^{o}C [9]. Nevertheless, the AFAs with Ti for γ'-Ni_3(Al,Ti) precipitates were not extensively studied for their creep and corrosion behaviour compared to the AFAs without Ti content. The Ti addition in AFAs should be further explored for the enhancement of their creep strength without sacrificing the beneficial Al_2O_3 formation in highly corrosive environments. Meanwhile, the authors have recently developed Fe-Ni-based austenitic alloys with increased Al (4.5 wt.%) and Ti (2–4 wt.%) content, in which the slightly increased Al content and addition of beneficial minor elements (C, B, and Zr) were considered to balance the detrimental effect of Ti on corrosion resistance [16]. The developed alloys were intended to deliver proper balance of creep resistance from the γ'-Ni_3(Al,Ti) precipitates and corrosion resistance from the protective Al_2O_3 layer in highly corrosive environments. The developed model alloy A with 4.5 wt.% Al and 3 wt.% Ti showed reasonable corrosion protection in the supercriticial-CO_2 (S-CO_2) environment at 650 ^{o}C and 20 MPa [17]. However, the corrosion behaviour in high temperature steam relevant to the A-USC plants was not evaluated. In this study, we have evaluated the performance of alloy A in aggressive steam environment at higher temperature of 750 ^{o}C for 1000 h, to determine its compatibility in water vapour environments. Accordingly, the effect of Ti on Al_2O_3 formation in steam environment is discussed. In addition, the effect of pre-oxidation treatment on steam corrosion resistance of alloy

A is also investigated, which was known to provide improved oxidation [18] and corrosion resistance [17, 19] at higher temperatures.

2. Materials and methodology

2.1. Test materials and specimen preparation

The nominal chemical composition of alloy A is provided in Table 1. The alloying elements were mixed and melted by vacuum arc remelting technique in Ar atmosphere, and cast as an ingot of 1.2 kg. The ingot was homogenized in air at 1150 ^{o}C for 1 h and hot-rolled with 60 % reduction in thickness followed by water quenching. The hot-rolled plate was solution annealed in air at 1150 ^{o}C for 2 h followed by water quenching. The solution annealed plate was then machined and cold-rolled for 10 % reduction in thickness to promote precipitate formation during creep tests. The final form of this wrought alloy is denoted as as-rolled condition. The chemical composition of the as-rolled alloy A was measured with carbon/sulphur analyser for carbon, nitrogen analyser for nitrogen and inductively coupled plasma atomic emission spectrometry for the remaining elements, and the results are shown in Table 1. The nitrogen was not intentionally added and present in small quantity, which was supposedly diffused into the alloy during the thermo-mechanical treatment in air. For the microstructural analysis, the as-rolled alloy A specimens were ground and final polished with 1 μm diamond paste. Coupon specimens were fabricated as dimensions of 6 mm in diameter and 1 mm in thickness, with a hole of 1.4 mm diameter for hanging the specimens. Before the corrosion tests, the coupon specimens were mechanically ground with #600 grit silicon carbide paper and cleaned ultrasonically in ethanol.

Table 1. Chemical composition in wt.% for the alloy A.

	Fe	Ni	Cr	Al	Ti	Nb	Si	Zr	C	B	N
Nominal	40.1	35	16	4.5	3	1	0.2	0.075	0.075	0.01	-
Measured	39.73	35.45	16.05	4.31	3.09	0.99	0.21	0.075	0.0844	0.01	0.0026

2.2. Pre-oxidation treatment and steam corrosion test

Pre-oxidation treatment was performed in laboratory air at 750 ^{o}C for 100 h for two of the ground and cleaned as-rolled coupon specimens. For the pre-oxidation treatment, the coupon specimens were hung in a platinum wire separated with alumina spacers and kept in an alumina boat. The steam corrosion test was conducted for three as-rolled specimens and two pre-oxidized specimens at 750 ^{o}C and 0.1 MPa for 1000 h. For the steam corrosion test, the coupon specimens were hung in a platinum wire and kept inside the test zone of a quartz tube placed in a furnace. The test zone of the quartz tube was maintained at the target temperature of 750 ^{o}C. The distilled water containing dissolved oxygen content less than 150 ppb was pumped into the system with a flow rate of 20 ml/min. The detailed description of the steam test equipment setup can be found in our previous publications [20, 21]. The specimens corroded in steam are indicated as A-AR and A-PO for the as-rolled and pre-oxidized specimens respectively.

2.3. Characterization of specimens and oxide layer

The weight of the coupon specimens was measured using a microbalance (Mettler Toledo AT20 Comparator) of resolution 0.001 mg before and after the corrosion tests. The average and standard deviation were calculated using the measured values of all the specimens. The microstructural analysis was conducted using scanning electron microscope (SEM, Hitachi SU5000) in the backscattered electrons (BSE) mode. The elemental composition of the phases was determined by energy dispersive X-ray spectrometer (EDS, Oxford instrument) from SEM analysis. Meanwhile, the surface oxide layer was analysed using secondary electrons (SE) mode in SEM analysis. For the microstructural analysis of the as-rolled alloy A by transmission electron microscopy (TEM), thin foil specimens of diameter 3 mm were prepared and ground down to a thickness of 100 μm. It was then followed by twin-jet electro-polishing with a solution of methanol and perchloric acid (9:1 ration) at 20 V and -30 ^{o}C. The focused ion beam (FIB, FEI Helios Nanolab 450 F1) was used for the preparation of TEM lamella containing the oxide scale. The TEM analysis was performed in the scanning transmission electron microscope (STEM) imaging mode using FEI Talos F200X at 200 kV. The TEM was equipped with high angle angular dark field (STEM-HAADF) detector and energy dispersive X-ray spectrometer (STEM-EDS, Super-X EDX detector). The structure of the phases was identified either by selected area diffraction (SAD) pattern or high-resolution transmission electron microscopy (HRTEM) mode coupled with the fast Fourier transform (FFT) processing technique. X-ray diffraction analysis (XRD, RIGAKU D/MAX-2500) at glancing angle was performed on surface oxide after the steam corrosion test. The cross-sectional oxide characterization was conducted by SEM-BSE analysis, in which the corroded coupon specimen was cut, ground, and polished with 1 μm diamond paste. The

equilibrium oxygen partial pressure (pO_2) of the corroding environments and metal oxides were calculated from Thermo-Calc program with TCFE9 database.

3. Results

3.1. Microstructure and pre-oxidation treatment

The SEM-BSE microstructural analysis of the as-rolled alloy A is shown in Fig. 1a. The microstructure consists of austenite matrix and dark phases of coarse blocky morphology. From the STEM-EDS line scan analysis and SAD pattern in Fig. 2, the coarse phases were identified as B2-NiAl phase. The average composition of the austenite matrix and coarse B2-NiAl phases measured from SEM-EDS analysis are given in Table 2. The coarse B2-NiAl phases constituted an area fraction of 7.8 % and average width of 6.4 μm. In our previous study, the coarse B2-NiAl phases occurred as a result of micro-segregation of Al and Ti upon solidification, while the solution annealing partially dissolved those phases [16]. The presence of B2-NiAl phases after solution annealing could be attributed to somewhat high Ni, Al and Ti contents of Alloy A compared to other AFA alloys. Currently, we are adjusting the minor elements in order to reduce the fraction of micro-segregation during solidification. In addition, Ti-Nb-rich carbonitrides were present in the austenite matrix of width 1–2 μm with varying degree of elemental composition. The Ti-Nb-rich carbonitrides with lower fraction of Nb appeared darker in the SEM-BSE analysis. Meanwhile, the alloy A showed lower average weight gain of 0.03715 ± 0.00645 mg/cm^2 after the pre-oxidation treatment at 750 ^{o}C for 100 h in air. The SEM and TEM analysis were conducted for the pre-oxidized alloy A used in our previous study [17]. The surface of the pre-oxidized alloy A in

Fig. 1b show features of grinding stripes, indicating that thinner oxide was developed during the pre-oxidation treatment. The SEM-EDS analysis showed the enrichment of Al and O on the austenite matrix and coarse B2-NiAl phases, indicative of presence of the Al-rich oxide. Isolated particles of Ti-Nb-rich oxides were observed that could have evolved from the pre-existing Ti-Nb-rich carbonitrides.

Table 2. Average composition in wt.% from SEM-EDS analysis on the austenite matrix and coarse B2-NiAl phase in as-rolled alloy A.

Alloy	Phase	Fe	Ni	Cr	Al	Ti	Nb	Si	Zr
A	Matrix	42.4	31.6	18.4	4.0	2.9	0.5	0.2	0.02
	B2-NiAl phase	24.1	47.9	7.9	12.8	6.4	0.6	0.2	0.08

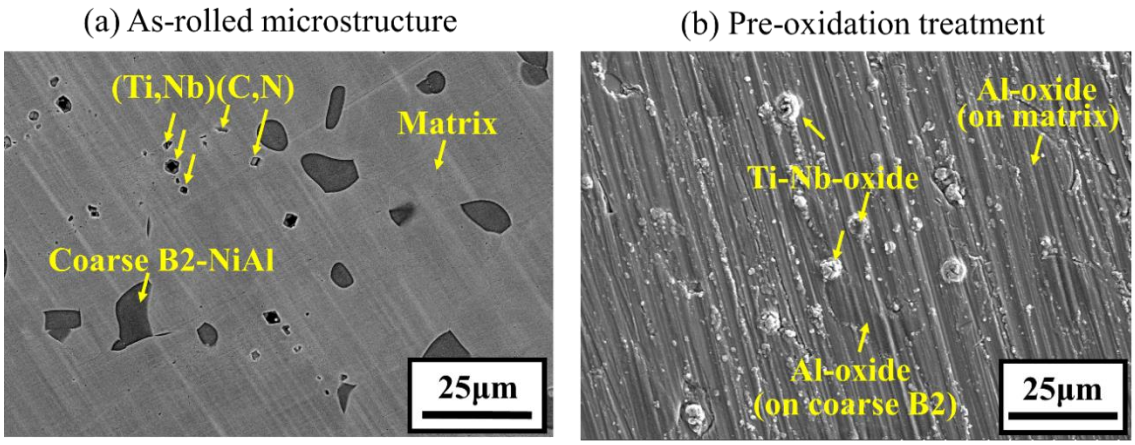

Figure 1. (a) SEM-BSE microstructure of as-rolled alloy A and (b) SEM-SE micrograph of as-rolled alloy A after the pre-oxidation treatment.

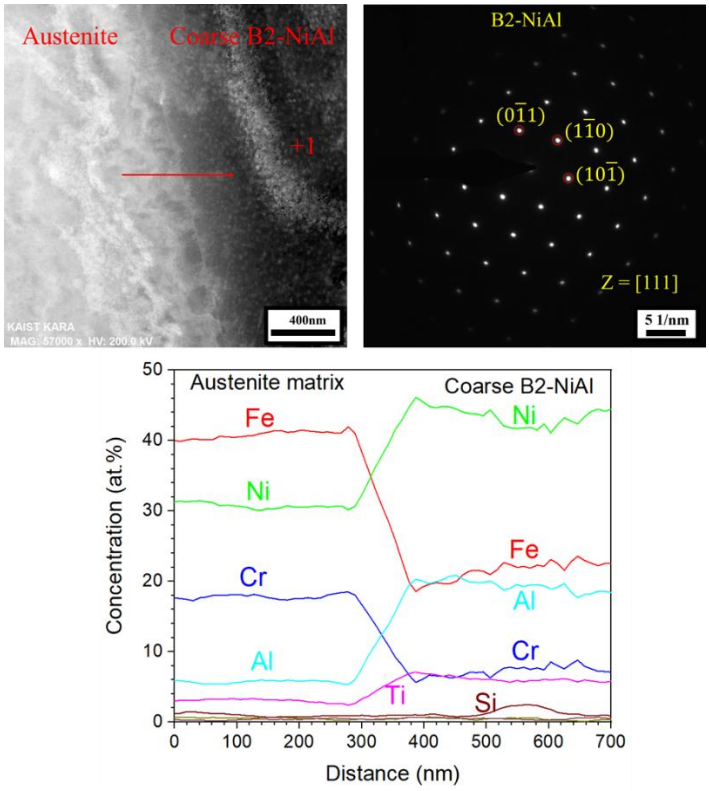

Figure 2. STEM-EDS line scan data with SAD pattern for the microstructural analysis in as-rolled alloy A.

The STEM-EDS analysis of the oxide layers formed after the pre-oxidation treatment of alloy A is shown in Fig. 3. The TEM micrograph showed thinner multilayered oxide structure, which formed externally over the austenite substrate. The oxide layer consisted of predominantly Al-oxide and intermediate Cr-rich oxide with an overall thickness of around 100 nm, of which the inner Al-oxide layer near the oxide-matrix interface is approximately 50 nm. SAD pattern on the multilayered oxide structure identified diffraction spots of α-Al_2O_3, γ-Al_2O_3, and $(Cr,Fe)_2O_3$ oxides. It was previously reported that for a similar oxide structure on a ferritic alumina-forming alloy [22], the outer Al-oxide layer was identified as γ-Al_2O_3 while the interfacial Al-oxide layer

as α-Al_2O_3. Accordingly, in this work, the outer Al-oxide layer is considered as γ-Al_2O_3, interfacial Al-oxide layer as α-Al_2O_3, and intermediate Cr-rich oxide as $(Cr,Fe)_2O_3$. In addition, Ti-Nb-nitrides can be located in the subsurface near the oxide-matrix interface, which occurred during the pre-oxidation treatment in air. Similarly, the presence of subsurface Ti-nitrides was previously observed for high Ti-containing austenitic alloys after high temperature air oxidation [23]. No Cr-depletion was identified beneath the oxide layer, while minor Al-depletion in the form of γ'-$Ni_3(Al,Ti)$ denuded region of depth around 50 nm was present.

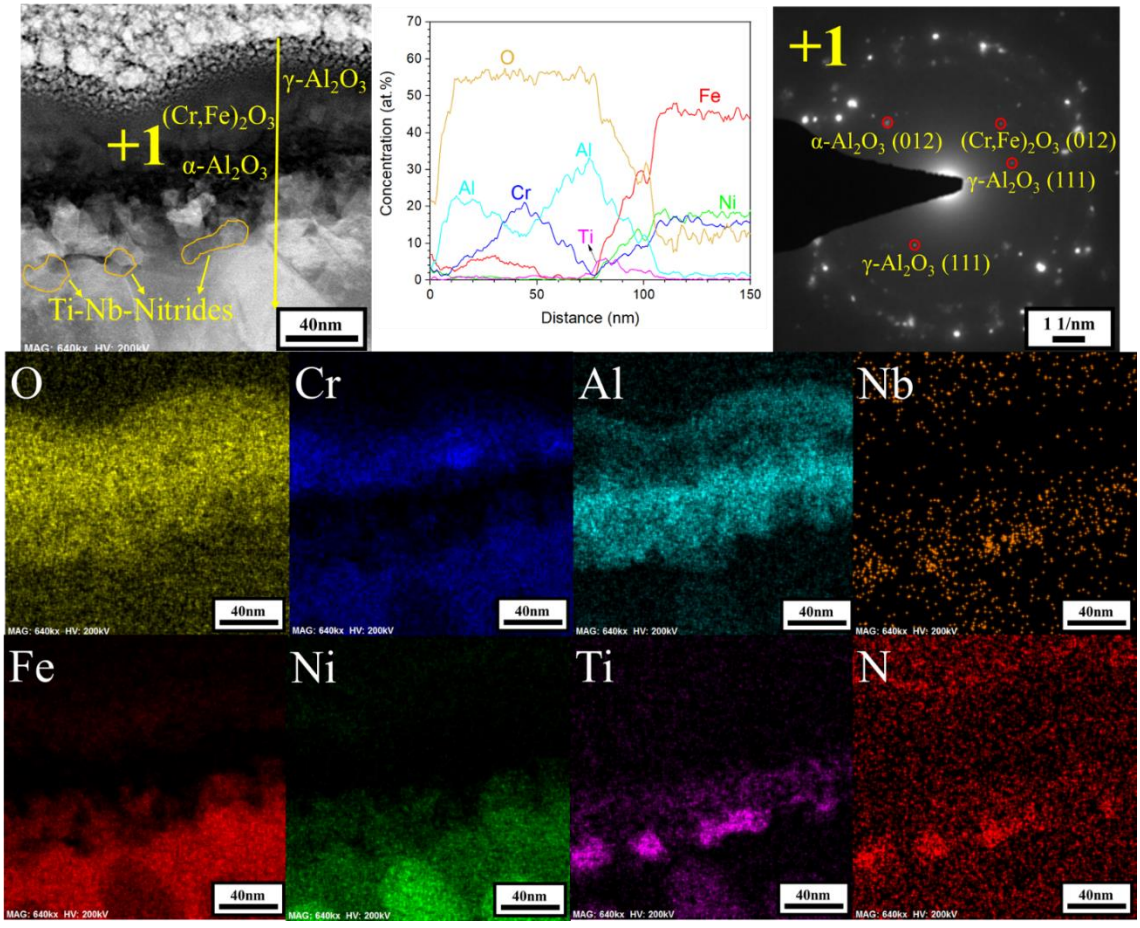

Figure 3. STEM-EDS line scan and elemental mapping analysis with SAD pattern for the oxide layers on austenite matrix of as-rolled alloy A after the pre-oxidation treatment.

3.2. Steam corrosion behaviour

The weight gain of the coupon specimens after the steam corrosion test at 750 ^{o}C for 1000 h is shown in Fig. 4. The A-PO showed considerably reduced weight gain than A-AR, suggesting better corrosion protection in steam environment. Nevertheless, the relatively higher weight gain of 0.23 mg/cm^2 for A-AR can still be considered as reasonably corrosion resistant for the steam corrosion test at 750 ^{o}C for 1000 h, compared to the other alumina-forming alloys [10]. The SEM-SE analysis of A-AR in Fig. 5a shows the presence of Cr-oxide layer predominantly covering the surface area, while some depressed regions were present sporadically. The depressed regions show enrichment of Al and O from the SEM-EDS analysis, indicative of Al-oxide. It was identified from the TEM analysis (later, Figs. 8 and 9) that thinner Al-oxide was developed on the coarse B2-NiAl phases observed in the as-rolled microstructure (Fig. 1a), while Cr-oxide was formed on the austenite matrix. Though the surface oxide morphology of A-AR was inhomogeneous, no deterioration of the oxide scale in the form of oxide layer spallation or breakaway corrosion was observed. In the case of A-PO (Fig. 5b), the surface morphology is comparable to the pre-oxidized alloy A before the steam corrosion test (Fig. 1b). The surface morphology shows features of grinding stripes, indicating that thicker oxides were not formed during the steam corrosion, which explains the lower weight gain (Fig. 4). The SEM-EDS analysis showed the presence of Al-oxide on both the matrix and coarse B2-NiAl phase for A-PO. Further growth and Al-enrichment occurred for the isolated particles during steam corrosion of A-PO, which are indicated as Ti-Al-Nb-rich oxide in Fig. 5b.

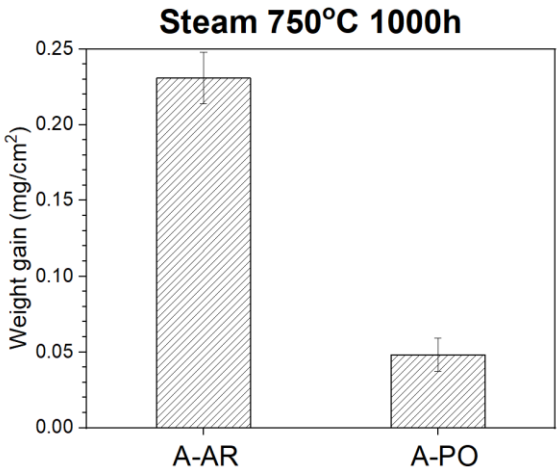

Figure 4. Weight gain of A-AR and A-PO after the steam corrosion test.

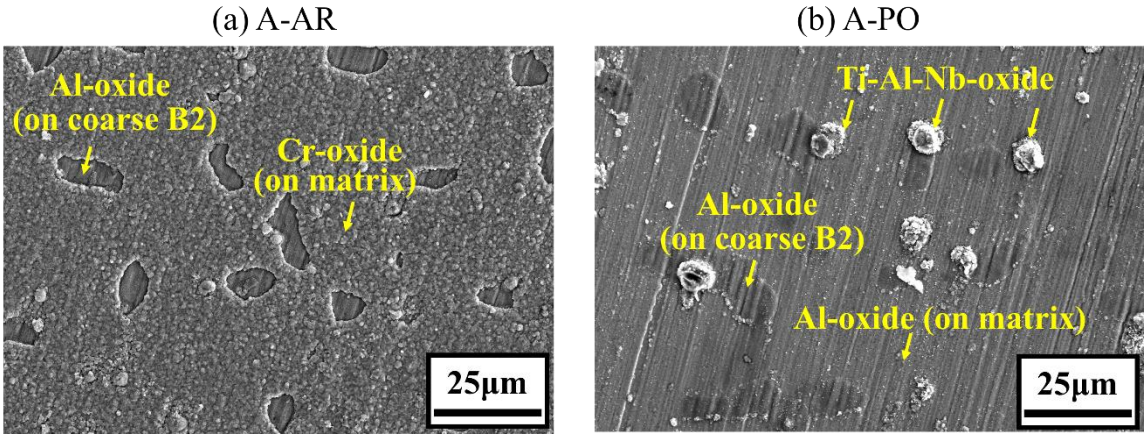

Figure 5. SEM-SE micrographs of (a) A-AR and (b) A-PO after the steam corrosion test.

The XRD results of surface oxide layer on A-AR and A-PO after the steam corrosion test are shown in Fig. 6. The A-AR show XRD peaks of Cr_2O_3, γ-Al_2O_3, and TiO_2 oxides along with the peaks of austenite matrix. The major Cr_2O_3 peaks can be associated with the Cr-oxide layer formed on the austenite matrix in Fig. 5a, while the identification of source for γ-Al_2O_3 and TiO_2

oxide peaks require detailed analyses. On the other hand, the A-PO exhibits predominantly austenite peaks with minor peaks of Cr_2O_3, sigma phase, and TiO_2. Only the (030) peak of α-Al_2O_3 was observed, in which the reduced intensity can be attributed to its smaller thickness and reduced diffraction signal from Al_2O_3 compared to the Cr_2O_3 [24]. The reduced intensity of oxide peaks in A-PO indicates the presence of thinner oxides after the steam corrosion test. The sigma phase was previously observed within the B2-NiAl phases during creep testing at 750 ^oC [16], and similar precipitation would have occurred in alloy A during the corrosion tests at 750 ^oC. Meanwhile, the peaks of sigma phase were not observed in A-AR, which could be attributed to the limited X-ray penetration into the matrix due to the relatively thick oxides of A-AR. The surface morphology and XRD result of A-PO after steam corrosion is comparable to the A-PO after S-CO_2 corrosion test [17], confirming that the pre-oxidation treatment provided better protection in both S-CO_2 and steam environments.

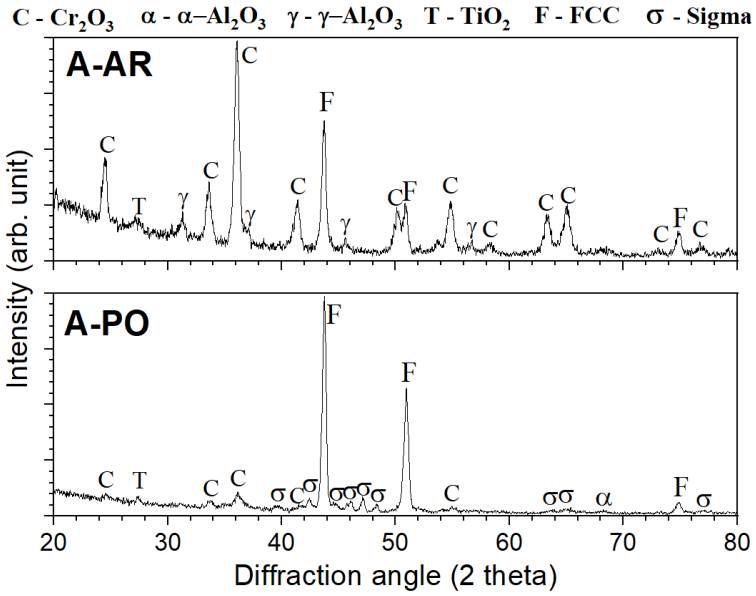

Figure 6. XRD results of A-AR and A-PO after the steam corrosion test.

The cross-sectional SEM-BSE micrograph of A-AR (Fig. 7a) shows the development of external Cr-oxide layer over the austenite substrate. In addition, internal Al-oxides were found inside the austenite subsurface as either discrete precipitates or a semi-continuous layer. Within the bulk austenite matrix, the coarse B2-NiAl phases decomposed internally into secondary austenite and sigma phases, similar to the previous observation during creep test at 750 ^{o}C [16]. Moreover, needle-like B2-NiAl phases precipitated inside the bulk austenite matrix during the steam corrosion, similar to the precipitation during creep test at 750 ^{o}C [16]. A B2-NiAl denuded region existed beneath the internal Al-oxides, indicating their dissolution to facilitate the Al supply for the internal Al-oxide formation. Meanwhile, the STEM-HAADF micrograph (Fig. 7b) showed the development of thinner Al-oxide layer over Ni-Al-Ti-enriched regions. It seems that the coarse B2-NiAl phases present at the surface disintegrated into Ni-Al-Ti-rich phases during the steam corrosion test, and will be further studied using STEM-EDS analysis in the next section.

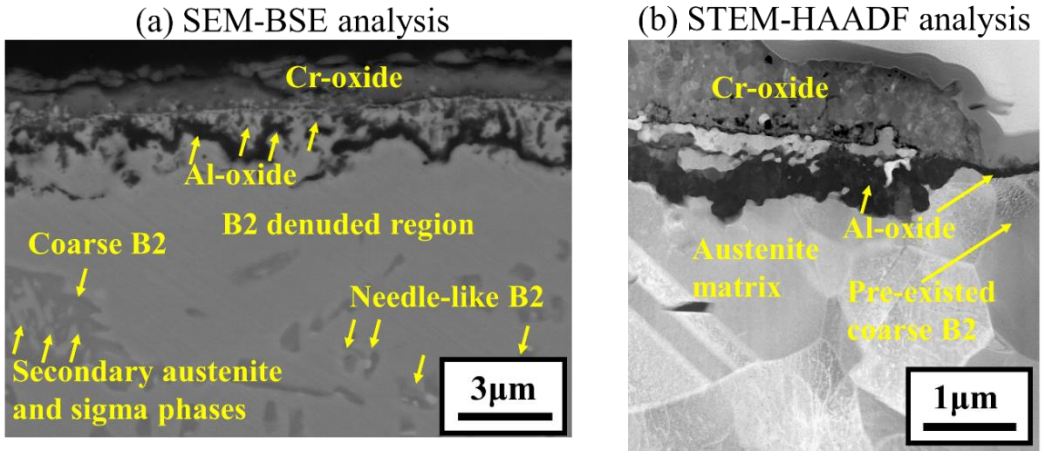

Figure 7. Cross-sectional (a) SEM-BSE and (b) STEM-HAADF micrographs of A-AR after the steam corrosion test.

3.3. Steam corrosion – TEM analysis

The STEM-EDS analysis of steam-corroded A-AR (Fig. 8) shows that the external Cr-oxide layer with an average thickness of around 1000 nm was formed over the austenite substrate. The continuous section of internal Al-oxide layer in the austenite subsurface exhibited a thickness around 500 nm. Austenite phase enriched with Fe and Ni (depleted of Cr and Al) of few hundred nm thick was present in the intermediate region between the external Cr-oxide and internal Al-oxide layer. Based on the SAD patterns (+1 and +2), the external Cr-oxide was identified as Cr_2O_3 and internal Al-oxide as γ-Al_2O_3. Ti-enriched oxides can be observed in the outer region of Cr_2O_3 layer and beneath the intermediate Fe-Ni-matrix region, while some Ti-incorporation was present within the Cr_2O_3 layer. Further analysis on the Ti-enriched oxide in the outer region of Cr_2O_3 layer by HRTEM-FFT pattern (+3) identified it as TiO_2, corresponding to the TiO_2 peaks from the XRD analysis (Fig. 6). Internally, few Ti-enriched oxides were observed that were connected with the outer region of internal Al-oxide layer (L2). However, it was difficult to identify the structure of the internal Ti-enriched oxides as they were superimposed with the internal Al-oxide layer in the 2D projections of TEM specimen. On the other hand, single-layered Al-oxide was identified externally over the pre-existed coarse B2-NiAl phase (Fig. 9). The SAD pattern showed only the diffraction spots of γ-Al_2O_3 without any noticeable $(Cr,Al)_2O_3$ oxide spots, though there was a slight presence of Cr in the outer region. It can be observed from Fig. 9 that the pre-existed coarse B2-NiAl phase closer to the exposed surface disintegrated into Fe-Ni-Cr-enriched and Ni-Al-Ti-enriched regions. From the compositional analysis and SAD patterns in Fig. 10, the Fe-Ni-Cr-enriched region was identified as austenite phase and the Ni-Al-Ti-enriched region as γ'-Ni_3(Al,Ti) phase.

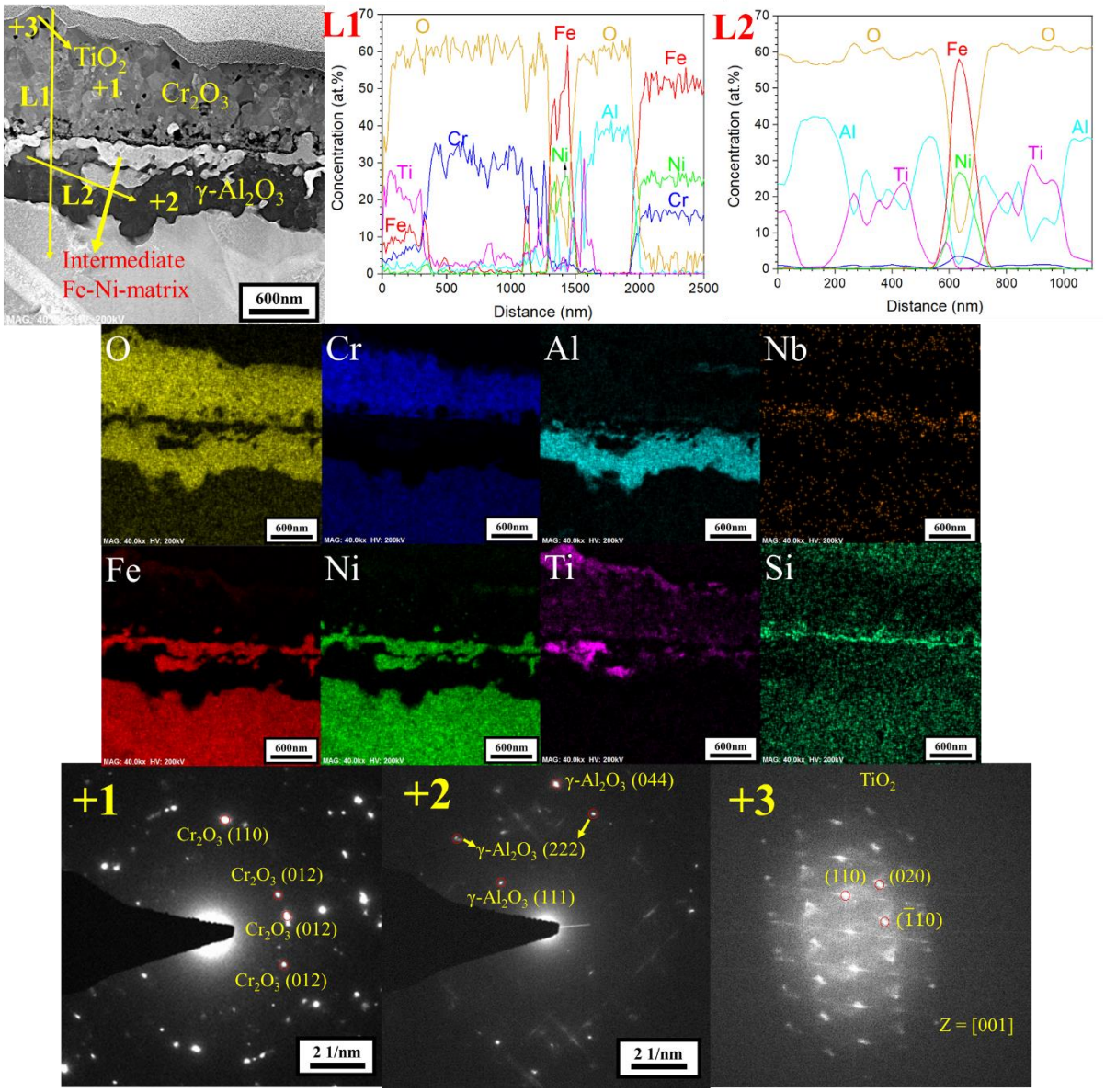

Figure 8. STEM-EDS line scan and elemental mapping analysis with SAD and HRTEM-FFT patterns for the oxide layers on austenite matrix of A-AR after the steam corrosion test.

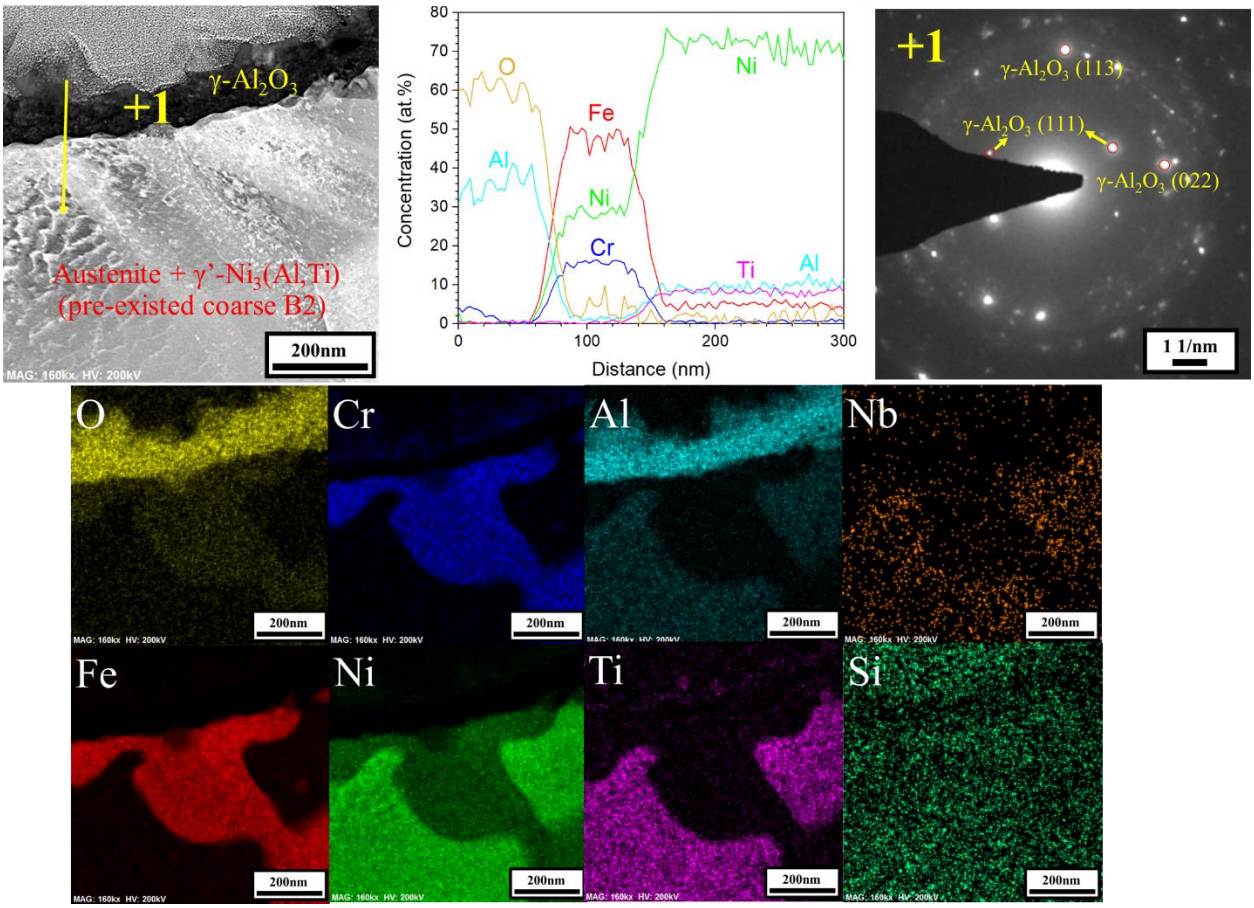

Figure 9. STEM-EDS line scan and elemental mapping analysis with SAD pattern for the oxide layers on pre-existed coarse B2-NiAl phase of A-AR after the steam corrosion test.

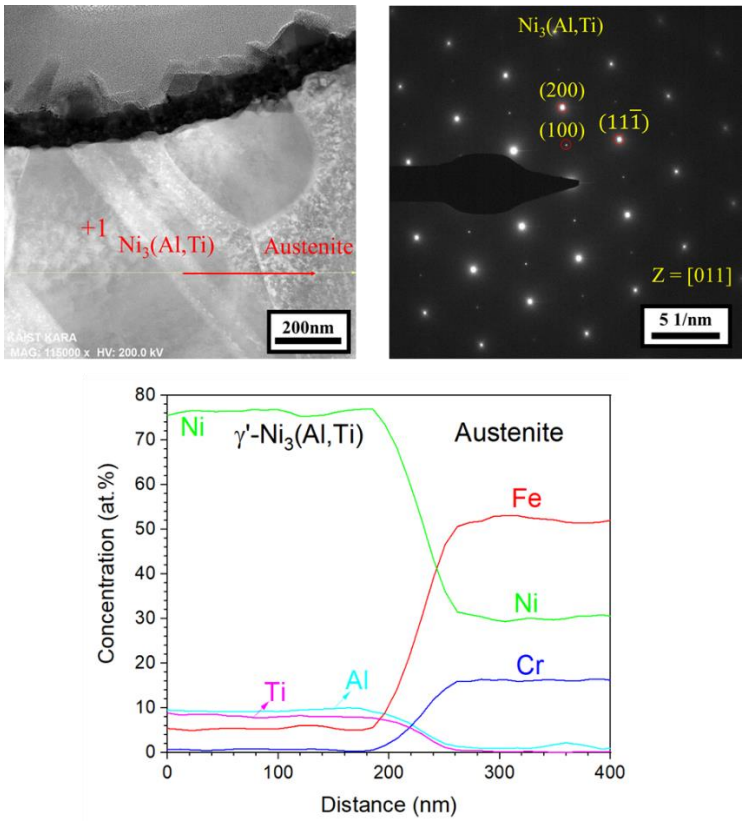

Figure 10. STEM-EDS line scan data with SAD pattern for the microstructural analysis in A-AR after the steam corrosion test.

For the A-PO, the STEM-EDS analysis in Fig. 11 shows the predominant presence of Al-oxide and intermediate Cr-rich oxides with an overall thickness of around 200 nm. The multilayered oxide structure of A-PO maintained the initial oxide morphology from the pre-oxidation treatment (Fig. 3), other than the slight inward thickening of the interfacial Al_2O_3 layer to around 100 nm for the steam-corroded specimen. Meanwhile, the concentration of O around the intermediate Cr-rich oxides occasionally dropped to some extent from the STEM-EDS line scan analysis. This would indicate the presence of some unoxidized metal particles incorporated within the oxide layer, representing the original matrix surface before the surface oxide formation. The

SAD pattern of the multilayered oxide shows the presence of only α-Al_2O_3 and $(Cr,Fe)_2O_3$, without any noticeable diffraction spots of γ-Al_2O_3 that were previously detected before the steam corrosion test (Fig. 3). The Ti-Nb-nitrides previously observed at the subsurface (Fig. 3) are now present within the interfacial Al-oxide layer, because of the inward growth of the Al-oxide layer during the steam corrosion test. Nevertheless, the Ti-Nb-nitrides were not oxidized upon being enclosed by the interfacial Al-oxide. Cr-depletion was not present beneath the oxide layer, while it exhibited γ'-Ni_3(Al,Ti) denuded region of depth around 200 nm.

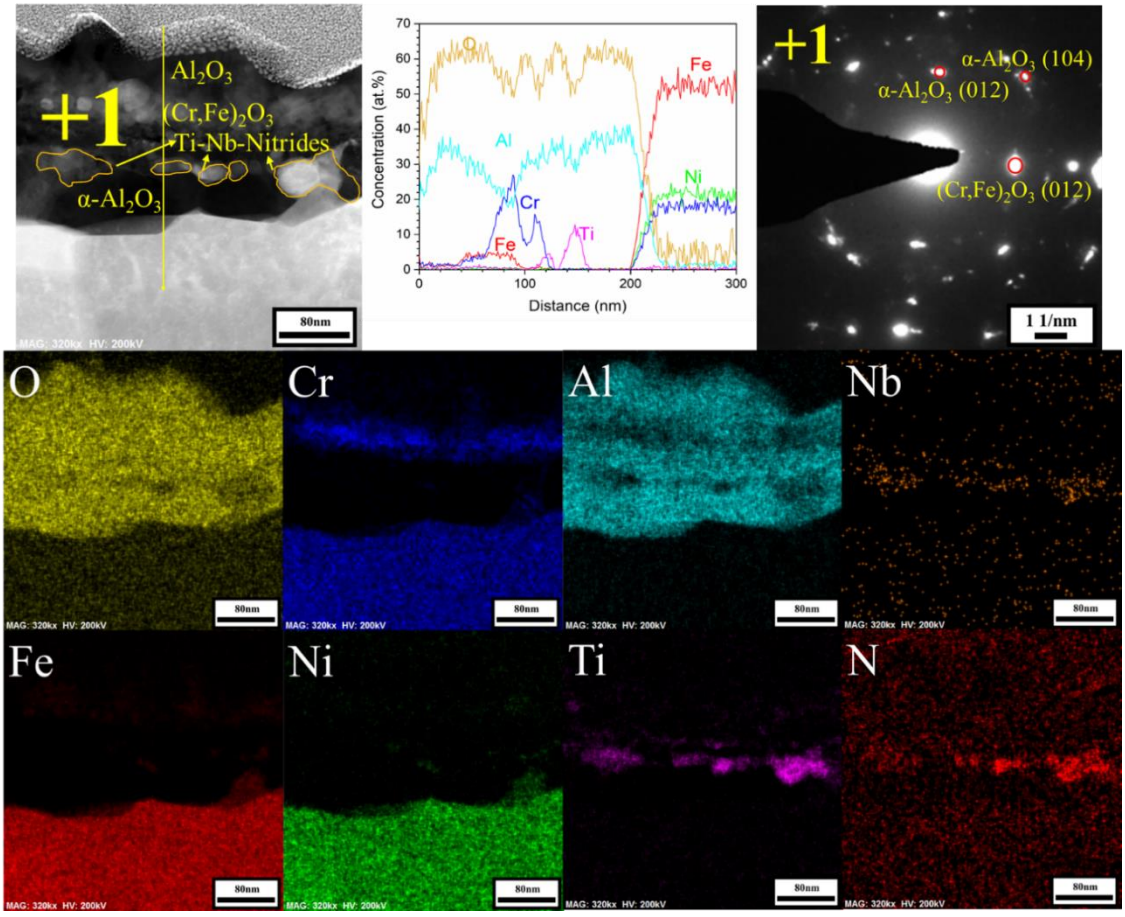

Figure 11. STEM-EDS line scan and elemental mapping analysis with SAD pattern for the oxide layers on austenite matrix of A-PO after the steam corrosion test.

4. Discussion

4.1. Steam corrosion

During the initial transient oxidation, the alloying elements at the exposed surface oxidize to form a transient oxide, followed by the development of stable and slower growing steady-state oxides [25]. Previously, Liu et al. [22] observed externally formed oxides with outer γ-Al_2O_3, intermediate Cr_2O_3, and interfacial α-Al_2O_3 layers on Kanthal AF alloy oxidized at 900 ^oC. In that case, the outer γ-Al_2O_3 and intermediate Cr_2O_3 were recognised as the remnants of initial transient oxides before the development of interfacial α-Al_2O_3 as steady-state oxide [22]. Similarly, the interfacial α-Al_2O_3 from alloy A pre-oxidized in air can be associated as the steady-state oxide, which reduced the growth of outer Al- and Cr-rich oxides (Fig. 3).

However, the oxide morphology of A-AR corroded in steam showed that the interfacial Al_2O_3 layer restricting the Cr_2O_3 growth was not established at the Cr_2O_3-matrix interface (Fig. 8). Instead, the inward diffusion of oxygen occurred leading to internal Al_2O_3 oxides, along with the continuous growth of external Cr_2O_3 layer. This oxide morphology of A-AR corroded in steam is also different from that of alloy A corroded in S-CO_2 [17], where the interfacial Al_2O_3 layer was established at the Cr_2O_3-matrix interface. The occurrence of external Cr_2O_3 and internal Al_2O_3 oxides for A-AR corroded in steam is comparable to the oxidation behaviour of Ni-Cr-Al alloys without sufficient Al content to form interfacial Al_2O_3 [26]. It indicates that the Al content in alloy A was lower than the critical concentration required for interfacial Al_2O_3 formation in steam environment, while it was enough for the air (Fig. 3) and S-CO_2 environment [17]. Additional

reactions occurring during the steam exposure must be accounted for this behaviour of A-AR. In comparison, the AFAs with a lower Al content of 2.5 wt.% managed to form protective Al_2O_3 layer in air [11] and air with 10 % water vapour environment [7] at 800 ^oC. The AFA with 3.5 wt.% Al in S-CO_2 environment at 650 ^oC and 20 MPa formed Al_2O_3 layer initially, however suffered from breakaway corrosion at later stages [27]. Moreover, 3.5 wt.% Al was sufficient to form stable Al_2O_3 layer in 1.7 MPa steam at a higher temperature of 800 ^oC [14]. Therefore, the non-occurrence of interfacial Al_2O_3 for A-AR in steam even with higher Al content (4.5 wt.%) must be associated with the additional presence of alloyed Ti. Eventually, the synergistic effect of steam and higher Ti content could have contributed towards the increased critical concentration of Al and retarding the interfacial alumina-forming capability of alloy A. The absence of either of these factors should have established the interfacial Al_2O_3 with improved corrosion protection.

The presence of water vapour or alloyed Ti was known to enhance the external Cr_2O_3 growth during high temperature corrosion. In the water vapour environment, Cr_2O_3 growth is promoted through various mechanisms such as hydrogen doping, modifications in chemical or transport behaviour in Cr_2O_3 [2]. Meanwhile, the Ti gets incorporated into Cr_2O_3 as Ti^{4+} ions substituting Cr^{3+} ions, thereby increasing the Cr-vacancies and accelerating the Cr_2O_3 growth [28]:

$$3TiO_2(+3Cr_2O_3) \rightarrow 3Ti_{Cr}^{*} + V_{Cr}^{'''} + 6O_O^x(+Cr_2O_3) \quad (1)$$

where, Ti_{Cr}^{*} is the presence of Ti-ions on Cr-lattice sites with single effective positive charge, $V_{Cr}^{'''}$ is the Cr-vacancy with triple effective negative charge, and O_O^x is the O-ion on O-lattice sites. It can be ascribed that a combination of mechanisms from the synergistic effect of steam and alloyed Ti promoted the external Cr_2O_3 growth for A-AR.

Meanwhile, the reasons for the additional occurrence of internal Al-oxidation in A-AR during steam corrosion is now discussed. According to the Wagner's theory, the critical concentration of alloying element required to form external over internal oxides decreases with the ambient oxygen potential [29, 30]. This is realised in the third element effect of Cr in alumina-forming alloys, where the transient Cr_2O_3 layer maintaining lower pO_2 (Fig. 12) at the Cr_2O_3-matrix interface enables easier formation of interfacial Al_2O_3 [31]. In our previous studies [17, 32], thin interfacial Al_2O_3 layer occurred beneath the Cr_2O_3 layer for austenitic heat resistant alloys with lower Al content (0.16–2 wt.%) in high temperature S-CO_2. On the other hand, those alloys showed internal Al_2O_3 oxides beneath the Cr_2O_3 layer when exposed to high temperature air [17, 33]. Furthermore, the heat resistant alloys also exhibited internal Al_2O_3 oxides during steam corrosion in our recent [34] and unpublished studies. The external Cr_2O_3 was present in all those cases, yet the internal Al_2O_3 oxides occurred under certain environments. It seems that the chemistry of the environment influences oxidizing conditions by altering the thermodynamics and/or kinetics of oxygen species at the oxide-matrix interface. The water vapour or steam environments are known to increase the susceptibility to internal oxidation likely from the ingress of hydrogen into the alloy subsurface [35]. The hydrogen ingress into the matrix from the wet environment eventually increases the oxygen permeability (solubility and diffusivity) compared to the dry environment [36, 37]. Moreover, Ti has higher affinity to oxygen similar to Al and contribute towards increased oxygen permeability in the matrix of Ti-alloys [38-40]. Notably, the Ti-Al alloys were unable to form protective Al_2O_3 layer at higher temperatures compared to Fe- and Ni-based alloys with Al [38]. Similar increase in oxygen permeability leading to internal oxidation of Al was reported for Ni-Fe-alloys [41], suggesting that presence of Ti could have contributed to the increased susceptibility of internal oxidation in alloy A. The absence of internal

oxidation in AFA OC4 alloy without Ti in 1.7 MPa steam at 800 °C [14], therefore, could validate the contribution of Ti on internal oxidation in alloy A. Consequently, the overall increase in oxygen permeability by steam and alloyed Ti supersedes the outward diffusion of subsurface Al towards the oxide-matrix interface, failing to establish the interfacial Al_2O_3 layer. The inwardly diffusing oxygen eventually arrives at the subsurface and internally forms discrete Ti-oxides and Al_2O_3 precipitates. The internal Al_2O_3 precipitates then grow laterally, coalescing to form continuous sections of Al_2O_3 oxide layer. Without the formation of interfacial Al_2O_3 layer at the Cr_2O_3-matrix interface, the Cr_2O_3 gradually grows and establishes as the steady-state oxide.

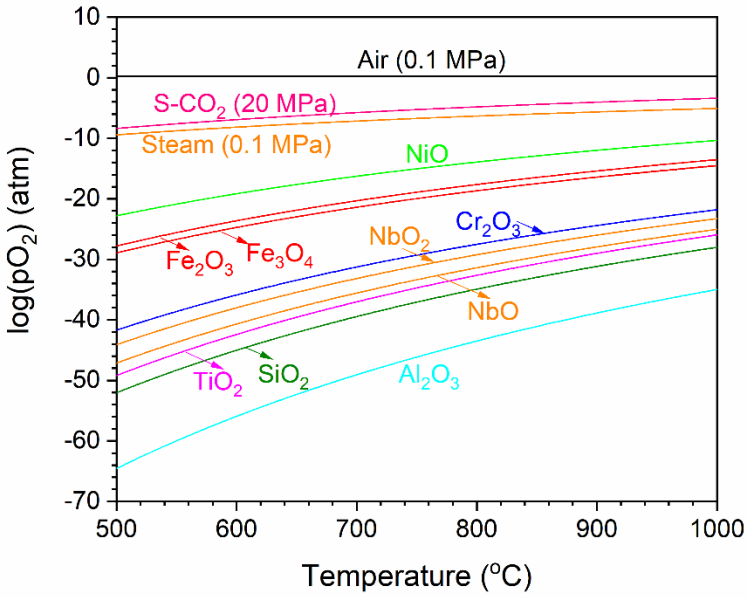

Figure 12. Equilibrium partial oxygen pressure calculated from Thermo-Calc program.

4.2. Oxide growth and subsurface morphology

Though the A-AR could not develop interfacial Al_2O_3 layer in steam environment, the thicknesses of external Cr_2O_3 and internal Al_2O_3 oxide layers were considerably lower than Ni-(16-18)Cr-1.8Al-2.4Ti alloys corroded in steam at 750 ^oC for 1000 h [42]. The thickness of external Cr_2O_3 layer and depth of internal Al_2O_3 oxides formed in those alloys were several times higher than A-AR. In addition, the internal Al_2O_3 oxides were found as discrete precipitates [42] compared to the predominantly continuous sections in A-AR (Fig. 7a). The higher Al content in alloy A facilitates extensive formation of internal Al_2O_3 precipitates, resulting in their earlier coalescence and formation of continuous sections of Al_2O_3 oxide layer. This continuous section of internal Al_2O_3 layer reduces the external Cr_2O_3 growth by restricting outward Cr diffusion from the underlying matrix in A-AR. It can be observed from the STEM-EDS line scan analysis (Fig. 8) that Cr-depletion was not present beneath the continuous section of internal Al_2O_3 layer, suggesting the restriction of outward Cr diffusion. Thereupon, the outward Cr diffusion would mostly occur through the austenite matrix located between the discontinuous sections of internal Al_2O_3 oxides. Eventually, the entirely connected Al_2O_3 layer would take over as the steady-state oxide and the corrosion rate would be limited by the transportation through this layer. Further occurrence of discrete Al_2O_3 precipitates were not regularly observed beneath the continuous sections of internal Al_2O_3 layer (Fig. 7), which establishes much lower oxygen potential (Fig. 12) over the underlying alloy and limits inward oxygen diffusion. The Al_2O_3 layer was also known to exhibit higher resistance to hydrogen permeability [43, 44]. In addition, the A-AR performed better than the reported Fe-Ni-based heat resistant alloy Sanicro 25 (22.6 wt.% Cr) corroded in water vapour environment, which showed excessive oxide growth and breakaway corrosion [45, 46]. The formation of interfacial Si-oxide (Fig. 8) along with the presence of beneficial minor elements

(C, B, and Zr) in alloy A would have also benefited the oxide adherence and growth rate, as it was reported in other studies [9, 47].

During the steam corrosion of A-AR, the continuous supply of subsurface Cr and Al to the respective external Cr_2O_3 and internal Al_2O_3 oxides depleted those elements in the subsurface region. Correspondingly, the intermediate matrix region was enriched with Fe and Ni that becomes sandwiched between the external and internal oxide layers. The Fe-Ni-matrix region remains unoxidized because of the oxygen potential maintained at the Cr_2O_3-matrix interface was much lower to stabilize Fe- and Ni-oxides (Fig. 12). It was reported that for the Ni-20Cr-3Al model alloy with similar oxide morphology to A-AR [26], further oxide growth at the later stages of oxidation leads to the interconnection of internal and external oxides, resulting in duplex oxide structure. Based on the STEM-EDS mapping analysis (Fig. 8), TiO_2 particle was observed over the Cr_2O_3 layer indicating that Ti ions diffused through the Cr_2O_3 layer and was oxidized at the surface. The Cr_2O_3 layer also contained Ti to some extent. This phenomenon was commonly observed for chromia-forming alloys with high Ti content, and was attributed towards the higher permeability of Ti ions in Cr_2O_3 [44, 48]. The interfacial Si-oxide in A-AR (Fig. 8) can be related with the SiO_2-type oxides occurring at the Cr_2O_3-matrix interface for chromia-forming alloys [47]. The SiO_2 oxide require much lower oxygen potential and is thermodynamically stable beneath the Cr_2O_3 layer (Fig. 12).

The coarse B2-NiAl phases are stabilised from the high temperature heat treatments and have reduced thermodynamic stability at lower temperatures [16]. In this study, we observed that the coarse B2-NiAl phases in the bulk matrix decompose internally into secondary austenite and sigma phases (Fig. 7a), similar to our previous observation during creep tests [16]. On the other hand, the coarse B2-NiAl phases on the exposed surface decomposes into austenite and γ'-

Ni_3(Al,Ti) phases during the steam corrosion (Figs. 9 and 10). It can be explained by the continuous Al-depletion to facilitate the formation of interfacial Al_2O_3 over that corresponding coarse B2-NiAl phase and internal Al_2O_3 in the adjacent austenite matrix. This continuous Al-depletion affects the chemical stability of coarse B2-NiAl phases, driving phase decomposition into the austenite and γ'-Ni_3(Al,Ti) phases. Similar transformation of the surface exposed B2-NiAl layer into γ'-Ni_3(Al,Ti) layer was previously observed for the aluminide coated specimens during the oxidation test [49].

4.3. α-Al_2O_3 transformation

The Al_2O_3 oxide exist as various metastable polymorphs (γ-, δ-, or θ-Al_2O_3) before its transformation towards the stable, slower-growing, and protective α-Al_2O_3. This structural transformation usually occurs at higher temperatures over 900 ^oC [50] or during prolonged exposure at lower temperatures. Meanwhile, the presence of adjacent corundum-type $(Cr,Fe)_2O_3$ oxides can assist as crystallographic templates for the nucleation of α-Al_2O_3 even at lower temperature of 700 ^oC [24, 51]. Therefore, it is supposed that the initial transient $(Cr,Fe)_2O_3$ oxides would have assisted as crystallographic templates for the development of α-Al_2O_3 during the air pre-oxidation treatment at 750 ^oC (Fig. 3). Moreover, the diffraction spots of γ-Al_2O_3 were not noticeably present after the steam corrosion test of A-PO (Fig. 11), suggesting that the gradual transformation of γ-Al_2O_3 to α-Al_2O_3 would have occurred during its exposure.

For the A-AR corroded in steam, the internal Al_2O_3 was identified as γ-Al_2O_3 polymorph and no instances of the stable α-Al_2O_3 phase were found based on the SAD pattern (Fig. 8). The internal Al_2O_3 oxides were also completely separated from the external Cr_2O_3 layer by the presence

of intermediate Fe-Ni-matrix, except at those austenite/B2-NiAl phase boundaries (Fig. 7b). The internal Al_2O_3 oxides being present as γ-Al_2O_3 polymorph could be because of the lack of adjacent $(Cr,Fe)_2O_3$ layers, acting as crystallographic template for the α-Al_2O_3 transformation. Moreover, the thinner Al_2O_3 oxide formed on the coarse B2-NiAl phase was also present as γ-Al_2O_3 polymorph, without any noticeable presence of adjacent $(Cr,Fe)_2O_3$ oxides (Fig. 9). Minor presence of Cr (~ 4 at.%) was observed in the outer region of γ-Al_2O_3 layer, yet corresponding diffraction spots of corundum-type oxides were not present. This could be because of minor Cr-incorporation in the outer γ-Al_2O_3 layer or insignificant fraction of corundum-type oxides that were not effective for rapid α-Al_2O_3 transformation in this case. In comparison, the presence of even lower Cr content (1 at.%) in B2-NiAl alloy was known to promote the α-Al_2O_3 oxides at 1000 ^oC in oxygen, where Cr-incorporation was present in the Al_2O_3 oxide [52]. Furthermore, the steam environment did not accelerate the α-Al_2O_3 transformation for the exposed γ-Al_2O_3 layer over the coarse B2-NiAl phases of A-AR. The influence of steam or water vapour environment on the α-Al_2O_3 transformation were not consistent from the reported studies [53]. Some researchers have observed the promoted transformation towards α-Al_2O_3 in water vapour environment [5, 6, 54], while other studies found the relative stabilization of γ-Al_2O_3 layer [22, 55, 56]. Nevertheless, the prolonged exposure in high temperature would gradually facilitate the α-Al_2O_3 transformation in A-AR.

4.4. Pre-oxidation treatment

The pre-formed oxide layer offered better corrosion protection with lower growth rate in steam environment without any occurrences of oxide failure. The steam exposure of the pre-

oxidized alloy A resulted in the slight inward growth (100 nm) of interfacial α-Al_2O_3 (Fig. 11) without any changes to the oxide morphology. The inward growth of α-Al_2O_3 encapsulated the Ti-Nb-nitrides, previously precipitated at the subsurface during pre-oxidation treatment (Fig. 3). The higher stability of the Ti-Nb-nitrides can be attributed to the lower oxygen potential from the encapsulating Al_2O_3 layer that was insufficient to stabilize Ti- and Nb-oxides (Fig. 12). In comparison, the pre-formed α-Al_2O_3 layer in alloy A also showed better corrosion protection in S-CO_2 without any issues of carburization or breakaway corrosion [17]. The oxide morphology from the pre-oxidation treatment was also maintained during the exposure to S-CO_2 [17], indicating that the pre-formed α-Al_2O_3 layer in alloy A exhibits higher degree of chemical stability in the studied high temperature environments.

Overall, it was identified that the pre-oxidation treatment of alumina-forming alloys could be a simple and effective surface treatment strategy for improved performance in corrosive high temperature environments. It is applicable for low temperature environments where the α-Al_2O_3 transformation is slower that results in metastable Al_2O_3 polymorphs offering lower protection. The pre-oxidation treatment can also be utilised for environments requiring increased critical Al concentration. Additionally, it neutralises the detrimental effect of high Ti content on corrosion resistance, promising balanced creep and corrosion resistance in alumina-forming alloys. Meanwhile, the oxide layer stability during long exposure periods and thermal-cycling conditions should be further evaluated for practical applications.

5. Conclusions

The corrosion behaviour of Fe-Ni-based alloy A (16Cr-4.5Al-3Ti, wt.%) in as-rolled and pre-oxidized conditions were evaluated in high temperature steam at 750 ^{o}C for 1000 h. The microstructure of as-rolled alloy A consisted of austenite matrix and coarse B2-NiAl phases. Based on the pre-oxidation and steam corrosion test, the following conclusions were drawn.

1. After the steam corrosion test, the as-rolled alloy A developed external Cr_2O_3 layer, intermediate Fe-Ni-matrix, and a semi-continuous internal γ-Al_2O_3 layer on the austenite matrix. The internal oxide formation was attributed to the increased oxygen permeability from the synergistic effect of steam and Ti, thereby increasing the critical Al concentration for interfacial Al_2O_3 formation.

2. Meanwhile, a thinner γ-Al_2O_3 layer was developed over the coarse B2-NiAl phases after the steam corrosion test. The coarse B2-NiAl phase at the exposed surface decomposed into austenite and γ'-Ni_3(Al,Ti) phases during the steam corrosion test, due to the continuous Al-depletion to facilitate Al_2O_3 formation.

3. The pre-oxidation treatment of alloy A in air at 750 ^{o}C for 100 h resulted in externally formed thinner oxides consisting of outer γ-Al_2O_3, intermediate $(Cr,Fe)_2O_3$, and interfacial α-Al_2O_3 layers on the austenite matrix. The coarse B2-NiAl phases also externally developed thinner Al-oxides during the pre-oxidation treatment.

4. The pre-oxidized alloy A showed improved steam corrosion protection with reduced weight gain. Also, the oxide morphology from pre-oxidation treatment was maintained, of which the interfacial α-Al_2O_3 layer slightly thickened during the steam corrosion.

Declaration of Competing Interest

The authors declare that they have no known competing financial interests or personal relationships that could have appeared to influence the work reported in this paper.

Data availability

The organized data are available upon request to the corresponding author.

CRediT authorship contribution statement

Gokul Obulan Subramanian: Conceptualization; Methodology; Investigation; Writing – original draft, **Chaewon Kim:** Investigation; Writing – review & editing, **Woong Heo:** Investigation, **Changheui Jang:** Methodology; Supervision; Writing – review & editing.

Acknowledgements

This study was mainly supported by the Nuclear R&D Program (no. 2016R1A5A101391921 and 2019M2D2A2050927) of the MSIT/NRF of the Rep. of Korea. Financial support for two of the authors is provided by the BK-Plus Program of the National Research Foundation (NRF) of the Rep. of Korea. The supports from the KAIST Analysis Center for Research Advancement (KARA) are acknowledged.

References

[1] A. Di Gianfrancesco, The fossil fuel power plants technology, in: A. Di Gianfrancesco (Ed.), Materials for Ultra-Supercritical and Advanced Ultra-Supercritical Power Plants, Woodhead Publishing, 2017, pp. 1-49. https://doi.org/10.1016/B978-0-08-100552-1.00001-4.

[2] D.J. Young, Effects of Water Vapour on Oxidation, in: D.J. Young (Ed.), High Temperature Oxidation and Corrosion of Metals, Second Edition, Elsevier Science, 2016, pp. 549-601. https://doi.org/10.1016/B978-0-08-100101-1.00011-X.

[3] S.H. Kim, J.-H. Cha, C. Jang, Corrosion and creep behavior of a Ni-base alloy in supercritical-carbon dioxide environment at 650 °C, Corros. Sci., 174 (2020) 108843. https://doi.org/10.1016/j.corsci.2020.108843.

[4] H. Hindam, D.P. Whittle, Microstructure, adhesion and growth kinetics of protective scales on metals and alloys, Oxid. Met., 18 (1982) 245-284. https://doi.org/10.1007/bf00656571.

[5] H. Buscail, S. Heinze, P. Dufour, J.P. Larpin, Water-vapor-effect on the oxidation of Fe-21.5 wt.%Cr-5.6 wt.%Al at 1000°C, Oxid. Met., 47 (1997) 445-464. https://doi.org/10.1007/BF02134786.

[6] S. Chevalier, P. Juzon, K. Przybylski, J.-P. Larpin, Water vapor effect on high-temperature oxidation behavior of Fe_3Al intermetallics, Science and Technology of Advanced Materials, 10 (2009) 045006. https://doi.org/10.1088/1468-6996/10/4/045006.

[7] Y. Yamamoto, M.P. Brady, Z.P. Lu, P.J. Maziasz, C.T. Liu, B.A. Pint, K.L. More, H.M. Meyer, E.A. Payzant, Creep-Resistant, Al_2O_3-Forming Austenitic Stainless Steels, Science, 316 (2007) 433. https://doi.org/10.1126/science.1137711.

[8] Y. Yamamoto, M.P. Brady, M.L. Santella, H. Bei, P.J. Maziasz, B.A. Pint, Overview of Strategies for High-Temperature Creep and Oxidation Resistance of Alumina-Forming Austenitic Stainless Steels, Metall. Mater. Trans. A, 42 (2011) 922-931. https://doi.org/10.1007/s11661-010-0295-2.

[9] Y. Yamamoto, G. Muralidharan, M.P. Brady, Development of L12-ordered Ni_3(Al,Ti)-strengthened alumina-forming austenitic stainless steel alloys, Scripta Mater., 69 (2013) 816-819. https://doi.org/10.1016/j.scriptamat.2013.09.005.

[10] M.P. Brady, J. Magee, Y. Yamamoto, D. Helmick, L. Wang, Co-optimization of wrought alumina-forming austenitic stainless steel composition ranges for high-temperature creep

and oxidation/corrosion resistance, Mater. Sci. Eng. A, 590 (2014) 101-115. https://doi.org/10.1016/j.msea.2013.10.014.

[11] M.P. Brady, Y. Yamamoto, M.L. Santella, B.A. Pint, Effects of minor alloy additions and oxidation temperature on protective alumina scale formation in creep-resistant austenitic stainless steels, Scripta Mater., 57 (2007) 1117-1120. https://doi.org/10.1016/j.scriptamat.2007.08.032.

[12] M.P. Brady, Y. Yamamoto, M.L. Santella, L.R. Walker, Composition, Microstructure, and Water Vapor Effects on Internal/External Oxidation of Alumina-Forming Austenitic Stainless Steels, Oxid. Met., 72 (2009) 311. https://doi.org/10.1007/s11085-009-9161-2.

[13] X. Xu, X. Zhang, G. Chen, Z. Lu, Improvement of high-temperature oxidation resistance and strength in alumina-forming austenitic stainless steels, Mater. Lett., 65 (2011) 3285-3288. https://doi.org/10.1016/j.matlet.2011.07.021.

[14] K.A. Unocic, M.P. Brady, B.A. Pint, A.R.-V. Put, Oxidation Behavior of Alumina-Forming Austenitic Steel, in: CORROSION 2013, NACE International, Orlando, Florida, 2013, pp. 11.

[15] B. Xiao, N. Tepylo, X. Huang, Z. Zhou, S. Penttilä, Oxidation Behavior of Alumina-Forming Austenitic Steels in Superheated Steam at 700 °C, Journal of Nuclear Engineering and Radiation Science, 6 (2020). https://doi.org/10.1115/1.4044530.

[16] G. Obulan Subramanian, C. Jang, J.H. Shin, C. Jeong, Effect of Ti Content on the Microstructure and High-Temperature Creep Property of Cast Fe-Ni-Based Alloys with High-Al Content, Materials, 14 (2021). https://doi.org/10.3390/ma14010082.

[17] G. Obulan Subramanian, S.H. Kim, J. Chen, C. Jang, Supercritical-CO_2 corrosion behavior of alumina- and chromia-forming heat resistant alloys with Ti, Corros. Sci., 188 (2021) 109531. https://doi.org/10.1016/j.corsci.2021.109531.

[18] A. Chyrkin, R. Pillai, T. Galiullin, E. Wessel, D. Grüner, W.J. Quadakkers, External α-Al_2O_3 scale on Ni-base alloy 602 CA. – Part I: Formation and long-term stability, Corros. Sci., 124 (2017) 138-149. https://doi.org/10.1016/j.corsci.2017.05.017.

[19] H.J. Lee, S.H. Kim, H. Kim, C. Jang, Corrosion and carburization behavior of Al-rich surface layer on Ni-base alloy in supercritical-carbon dioxide environment, Appl. Surf. Sci., 388 (2016) 483-490. https://doi.org/10.1016/j.apsusc.2015.11.162.

[20] S.H. Kim, C. Kim, J.-H. Cha, C. Jang, Y.S. Yoo, Effect of Minor Alloying Elements on the Oxidation Behavior of Ni-Base Alloys in a High-Temperature Steam Environment, Oxid. Met., 92 (2019) 505-523. https://doi.org/10.1007/s11085-019-09940-y.

[21] C. Kim, H. Kim, W. Heo, C. Jang, S.Y. Lee, S. Lee, J.-S. Lee, High-temperature steam oxidation behavior of alumina-forming duplex FeNiCrAl and ferritic FeCrAl alloys at 800 °C to 1050 °C, Corros. Sci., 190 (2021) 109658. https://doi.org/10.1016/j.corsci.2021.109658.

[22] F. Liu, H. Josefsson, J.-E. Svensson, L.-G. Johansson, M. Halvarsson, TEM investigation of the oxide scales formed on a FeCrAlRE alloy (Kanthal AF) at 900°C in dry O_2 and O_2 with 40% H_2O, Mater. High Temp., 22 (2005) 521-526. https://doi.org/10.1179/mht.2005.062.

[23] K. Wollgarten, T. Galiullin, W.J. Nowak, W.J. Quadakkers, D. Naumenko, Effect of alloying additions and presence of water vapour on short-term air oxidation behaviour of cast Ni-base superalloys, Corros. Sci., 173 (2020) 108774. https://doi.org/10.1016/j.corsci.2020.108774.

[24] H. Asteman, M. Spiegel, A comparison of the oxidation behaviours of Al_2O_3 formers and Cr_2O_3 formers at 700°C – Oxide solid solutions acting as a template for nucleation, Corros. Sci., 50 (2008) 1734-1743. https://doi.org/10.1016/j.corsci.2007.12.012.

[25] B. Chattopadhyay, G.C. Wood, The transient oxidation of alloys, Oxid. Met., 2 (1970) 373-399. https://doi.org/10.1007/BF00604477.

[26] C.S. Giggins, F.S. Pettit, Oxidation of Ni-Cr-Al Alloys Between 1000° and 1200°C, J. Electrochem. Soc., 118 (1971) 1782. https://doi.org/10.1149/1.2407837.

[27] L.-F. He, P. Roman, B. Leng, K. Sridharan, M. Anderson, T.R. Allen, Corrosion behavior of an alumina forming austenitic steel exposed to supercritical carbon dioxide, Corros. Sci., 82 (2014) 67-76. https://doi.org/10.1016/j.corsci.2013.12.023.

[28] A. Jalowicka, W. Nowak, D. Naumenko, L. Singheiser, W.J. Quadakkers, Effect of nickel base superalloy composition on oxidation resistance in SO_2 containing, high pO_2 environments, Mater. Corros., 65 (2014) 178-187. https://doi.org/10.1002/maco.201307299.

[29] C. Wagner, Reaktionstypen bei der Oxydation von Legierungen, Zeitschrift für Elektrochemie, Berichte der Bunsengesellschaft für physikalische Chemie, 63 (1959) 772-782. https://doi.org/10.1002/bbpc.19590630713.

[30] T.D. Nguyen, Y. Xie, S. Ding, J. Zhang, D.J. Young, Oxidation Behavior of Ni–Cr Alloys in CO_2 at 700 °C, Oxid. Met., 87 (2017) 605-616. https://doi.org/10.1007/s11085-017-9721-9.

[31] D.J. Young, Alloy Oxidation III: Multiphase Scales, in: D.J. Young (Ed.), High Temperature Oxidation and Corrosion of Metals, Second Edition, Elsevier Science, 2016, pp. 335-392. https://doi.org/10.1016/B978-0-08-100101-1.00007-8.

[32] H.J. Lee, H. Kim, S.H. Kim, C. Jang, Corrosion and carburization behavior of chromia-forming heat resistant alloys in a high-temperature supercritical-carbon dioxide environment, Corros. Sci., 99 (2015) 227-239. https://doi.org/10.1016/j.corsci.2015.07.007.

[33] G. Obulan Subramanian, S.H. Kim, C. Jang, The carburization behavior of alloy 800HT in high temperature supercritical-CO_2, Mater. Lett., 299 (2021) 130067. https://doi.org/10.1016/j.matlet.2021.130067.

[34] J. Chen, C. Jang, Q. Xiao, H.B. Lee, C. Kim, S.H. Kim, J.H. Shin, G. Obulan Subramanian, Effect of surface conditions and alloying elements on the early oxidation behaviour of two austenitic alloys in the pure steam environment, Appl. Surf. Sci., 563 (2021) 150314. https://doi.org/10.1016/j.apsusc.2021.150314.

[35] E. Essuman, G.H. Meier, J. Żurek, M. Hänsel, W.J. Quadakkers, The Effect of Water Vapor on Selective Oxidation of Fe–Cr Alloys, Oxid. Met., 69 (2008) 143-162. https://doi.org/10.1007/s11085-007-9090-x.

[36] M.H.B. Ani, T. Kodama, M. Ueda, K. Kawamura, T. Maruyama, The Effect of Water Vapor on High Temperature Oxidation of Fe–Cr Alloys at 1073 K, Mater. Trans., 50 (2009) 2656-2663. https://doi.org/10.2320/matertrans.M2009212.

[37] A.R. Setiawan, M. Hanafi Bin Ani, M. Ueda, K. Kawamura, T. Maruyama, Oxygen Permeability through Internal Oxidation Zone in Fe–Cr Alloys under Dry and Humid Conditions at 973 and 1073 K, ISIJ Int., 50 (2010) 259-263. https://doi.org/10.2355/isijinternational.50.259.

[38] R.A. Perkins, K.T. Chiang, G.H. Meier, Formation of alumina on Ti-Al alloys, Scripta Metallurgica, 21 (1987) 1505-1510. https://doi.org/10.1016/0036-9748(87)90291-2.

[39] H.J. Grabke, Oxidation of Aluminides, Mater. Sci. Forum, 251-254 (1997) 149-162. https://doi.org/10.4028/www.scientific.net/MSF.251-254.149.

[40] A. Donchev, M. Schütze, Minimization of the Oxygen Embrittlement of Ti-Alloys, in, Theodor-Heuss-Allee 25, 60486 Frankfurt am Main, 2010.

[41] H. Shi, C. Tang, A. Jianu, R. Fetzer, A. Weisenburger, M. Steinbrueck, M. Grosse, R. Stieglitz, G. Müller, Oxidation behavior and microstructure evolution of alumina-forming austenitic & high entropy alloys in steam environment at 1200 °C, Corros. Sci., 170 (2020) 108654. https://doi.org/10.1016/j.corsci.2020.108654.

[42] Y. Xu, J. Lu, W. Li, Z. Yang, Y. Gu, Chromium-Dependent Effect on Oxidation Behavior of Ni-Fe-Based Superalloy for Ultra-Supercritical Steam Turbine Applications: Influence of Temperature and Pure Steam, Corrosion, 76 (2020) 941-953. https://doi.org/10.5006/3534.

[43] J. Wang, Z. Lu, Y. Ling, R. Wang, Y. Li, Q. Zhou, Z. Zhang, Hydrogen permeation properties of $Cr_xC_y@Cr_2O_3/Al_2O_3$ composite coating derived from selective oxidation of a CrC alloy and atomic layer deposition, Int. J. Hydrogen Energy, 43 (2018) 21133-21141. https://doi.org/10.1016/j.ijhydene.2018.08.192.

[44] M. Abbasi, D.-I. Kim, J.-H. Shim, W.-S. Jung, Effects of alloyed aluminum and titanium on the oxidation behavior of INCONEL 740 superalloy, J. Alloys Compd., 658 (2016) 210-221. https://doi.org/10.1016/j.jallcom.2015.10.198.

[45] J. Zurek, S.-M. Yang, D.-Y. Lin, T. Hüttel, L. Singheiser, W.J. Quadakkers, Microstructural stability and oxidation behavior of Sanicro 25 during long-term steam exposure in the temperature range 600–750 °C, Mater. Corros., 66 (2015) 315-327. https://doi.org/10.1002/maco.201407901.

[46] L. Intiso, L.G. Johansson, J.E. Svensson, M. Halvarsson, Oxidation of Sanicro 25 (42Fe22Cr25NiWCuNbN) in O_2 and O_2 + H_2O Environments at 600–750 °C, Oxid. Met., 83 (2015) 367-391. https://doi.org/10.1007/s11085-015-9528-5.

[47] T.D. Nguyen, J. Zhang, D.J. Young, Effects of Si, Al and Ti on corrosion of Ni-20Cr and Ni-30Cr alloys in Ar-20CO_2-20H_2O gas at 700 °C, Corros. Sci., 170 (2020) 108702. https://doi.org/10.1016/j.corsci.2020.108702.

[48] S. Cruchley, H.E. Evans, M.P. Taylor, M.C. Hardy, S. Stekovic, Chromia layer growth on a Ni-based superalloy: Sub-parabolic kinetics and the role of titanium, Corros. Sci., 75 (2013) 58-66. https://doi.org/10.1016/j.corsci.2013.05.016.

[49] D. Kim, I. Sah, H.J. Lee, S. Hong, C. Jang, Development of an aluminide coating layer on Alloy 617 by Al sputtering and inter-diffusion heat treatments, Surf. Coat. Technol., 244 (2014) 15-22. https://doi.org/10.1016/j.surfcoat.2014.01.009.

[50] F.H. Stott, The Oxidation of Alumina-Forming Alloys, Mater. Sci. Forum, 251-254 (1997) 19-32. https://doi.org/10.4028/www.scientific.net/MSF.251-254.19.

[51] P. Brito, H. Pinto, A. Kostka, The crystallographic template effect assisting the formation of stable α-Al_2O_3 during low temperature oxidation of Fe–Al alloys, Corros. Sci., 105 (2016) 100-108. https://doi.org/10.1016/j.corsci.2016.01.007.

[52] R. Klumpes, C.H.M. Maree, E. Schramm, J.H.W.d. Wit, The influence of chromium on the oxidation of β-NiAl at 1000ºC, Mater. Corros., (1996) 619-624. https://doi.org/10.1002/maco.19960471105.

[53] D.J. Young, Oxidation of Alloys I: Single Phase Scales, in: D.J. Young (Ed.), High Temperature Oxidation and Corrosion of Metals, Second Edition, Elsevier Science, 2016, pp. 193-260. https://doi.org/10.1016/S1875-9491(08)00005-7.

[54] Z. Zhou, H. Guo, M. Abbas, S. Gong, Effect of water vapor on the phase transformation of alumina grown on NiAl at 950°C, Corros. Sci., 53 (2011) 2943-2947. https://doi.org/10.1016/j.corsci.2011.05.029.

[55] H. Götlind, F. Liu, J.E. Svensson, M. Halvarsson, L.G. Johansson, The Effect of Water Vapor on the Initial Stages of Oxidation of the FeCrAl Alloy Kanthal AF at 900 °C, Oxid. Met., 67 (2007) 251-266. https://doi.org/10.1007/s11085-007-9055-0.

[56] F. Liu, H. Götlind, J.-E. Svensson, L.-G. Johansson, M. Halvarsson, Early stages of the oxidation of a FeCrAlRE alloy (Kanthal AF) at 900°C: A detailed microstructural investigation, Corros. Sci., 50 (2008) 2272-2281. https://doi.org/10.1016/j.corsci.2008.05.019.